

Supporting Information

Amorphous FeNiCu-MOF as highly efficient electrocatalysts for oxygen evolution reaction in alkaline medium

Hao Wu^{a+}, Qingxi Zhai^{a+}, Fan Ding^b, Dongyue Sun^a, Yujie Ma^c, Yilun Ren^a, Biao Wang^a, Fengqi Li^a, Haifeng Bian^a, Yurong Yang^a, Lan Chen^a, Shaochun Tang^a, Xiangkang Meng^{a*}

^a *National Laboratory of Solid State Microstructures, Collaborative Innovation Center of Advanced Microstructures, College of Engineering and Applied Sciences, Nanjing University, Nanjing 210093, PR China*

^b *Department of Computer Science, Purdue University, West Lafayette, IN 47907, USA*

^c *School of Intelligent Manufacturing and Information, Jiangsu Shipping College, Nantong 226010, PR China*

⁺These authors contributed equally to this work.

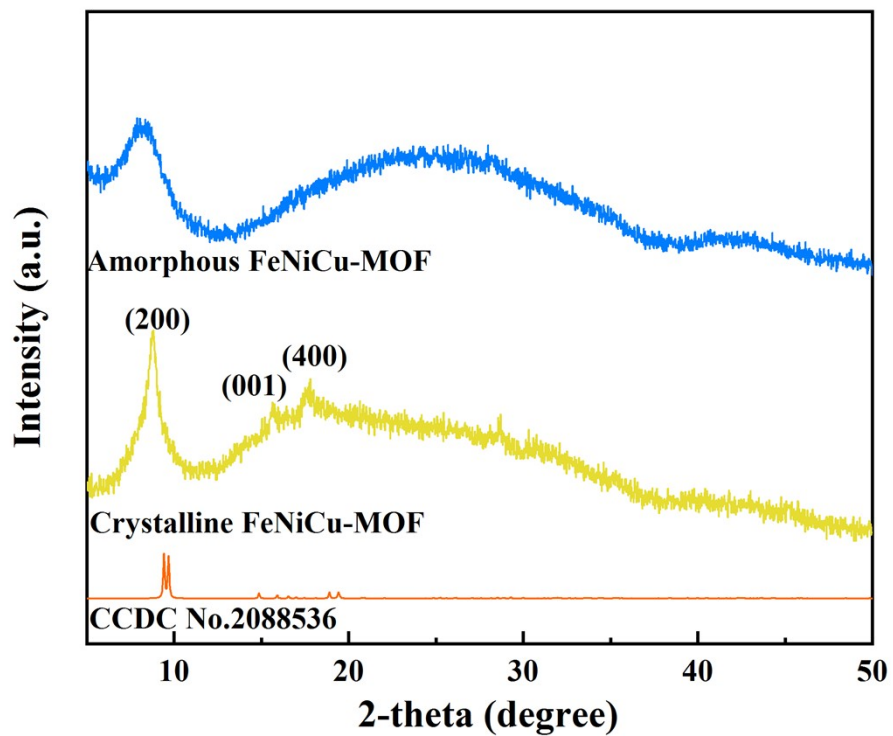


Fig. S1. XRD patterns of amorphous and crystalline FeNiCu-MOF.

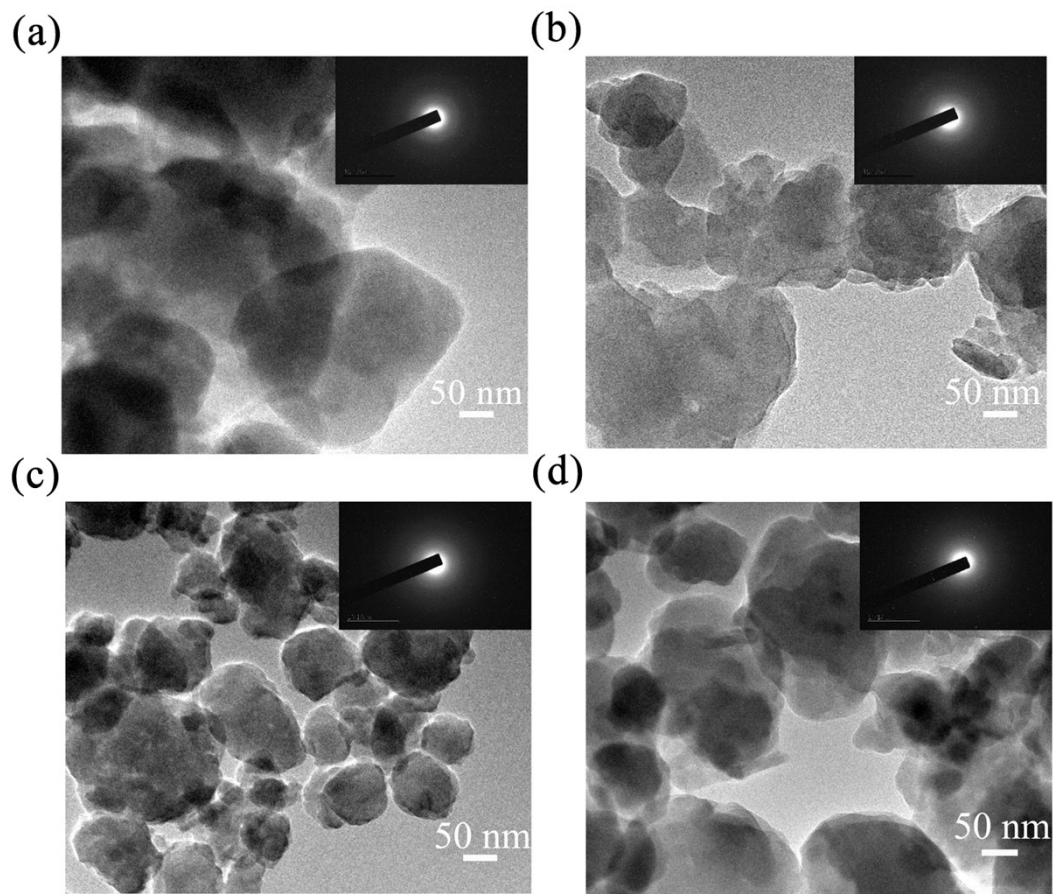


Fig. S2. High-magnification TEM image of (a) Fe_{0.6}(NiCu)_{2.4}-MOF, (b) Fe_{0.8}(NiCu)_{2.2}-MOF, (c) Fe_{1.2}(NiCu)_{1.8}-MOF and (d) Fe_{1.4}(NiCu)_{1.6}-MOF.

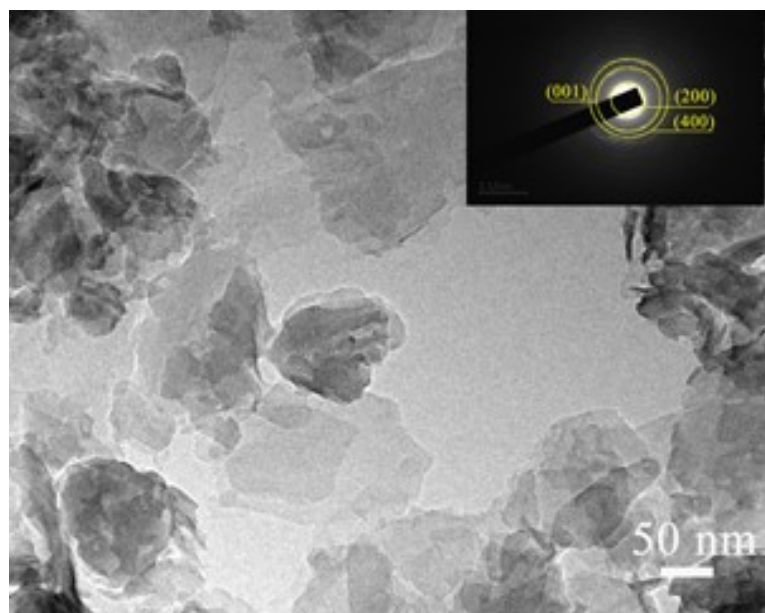


Fig. S3. High-magnification TEM image of crystalline FeNiCu-MOF.

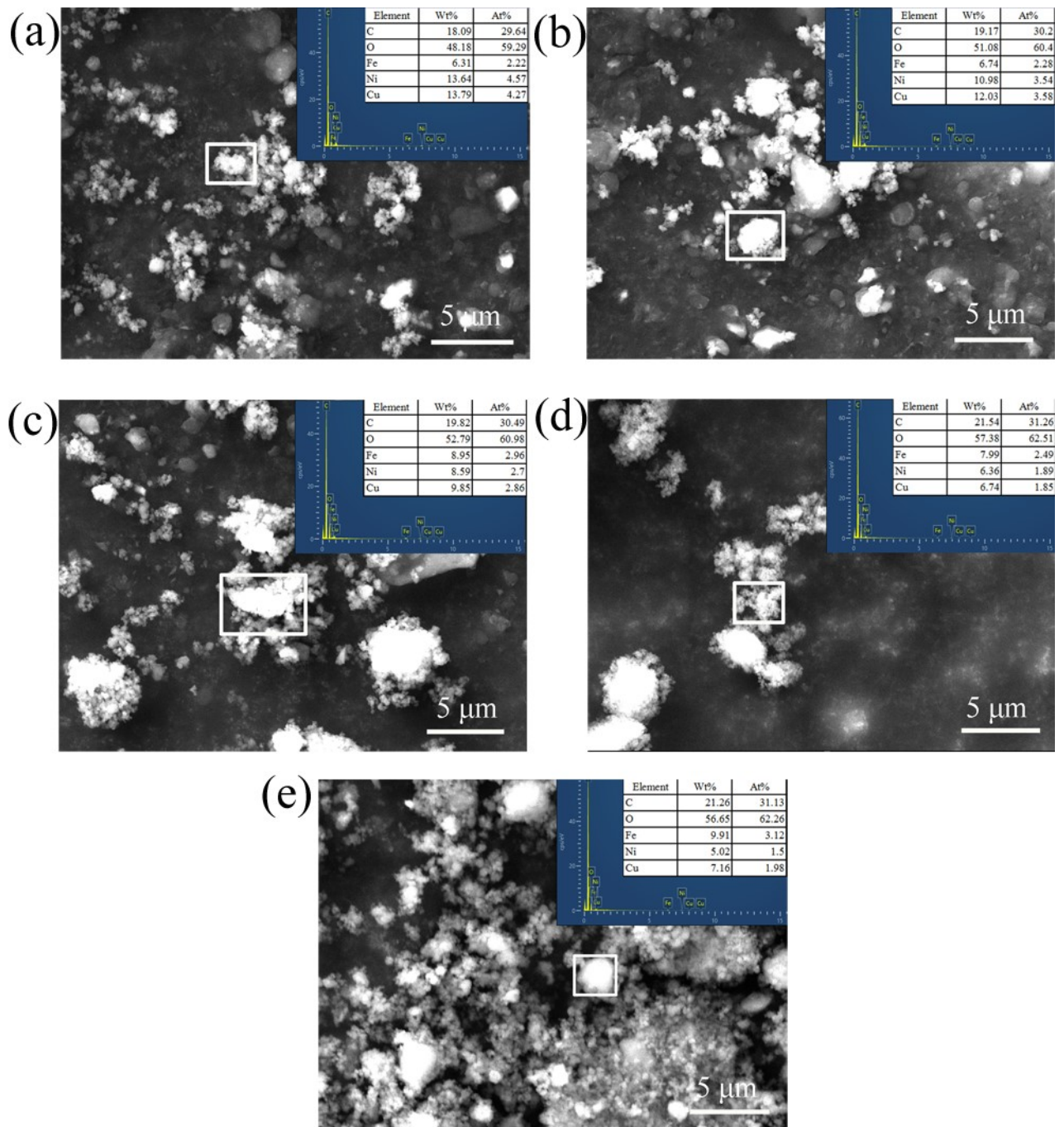


Fig. S4. SEM images with the corresponding EDS (inset) of (a) $\text{Fe}_{0.6}(\text{NiCu})_{2.4}$ -MOF, (b) $\text{Fe}_{0.8}(\text{NiCu})_{2.2}$ -MOF, (c) FeNiCu-MOF, (d) $\text{Fe}_{1.2}(\text{NiCu})_{1.8}$ -MOF and (e) $\text{Fe}_{1.4}(\text{NiCu})_{1.6}$ -MOF.

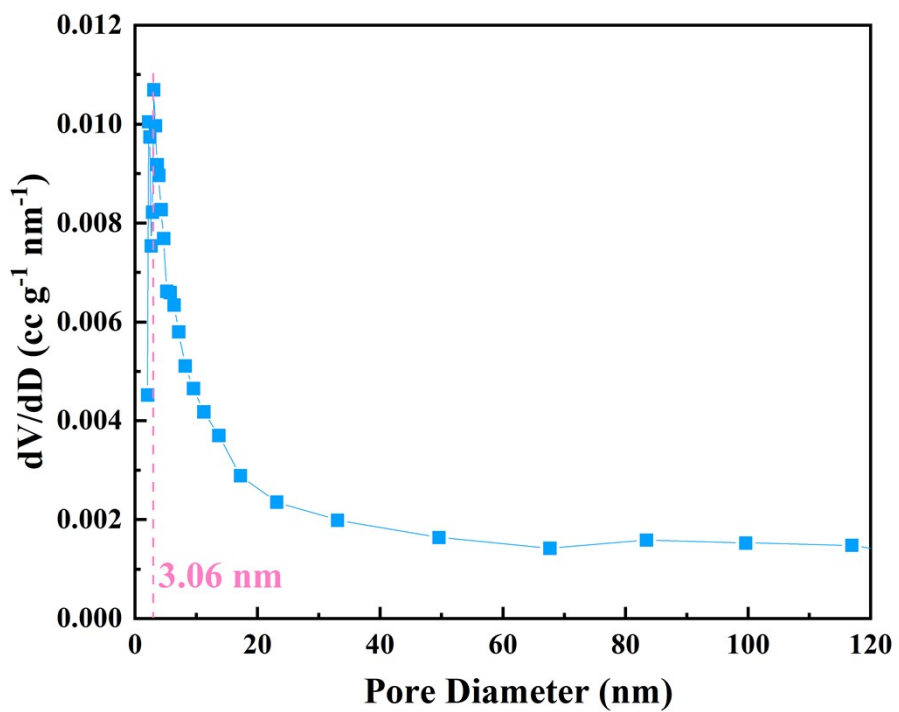


Fig. S5. Pore diameter distribution of FeNiCu-MOF.

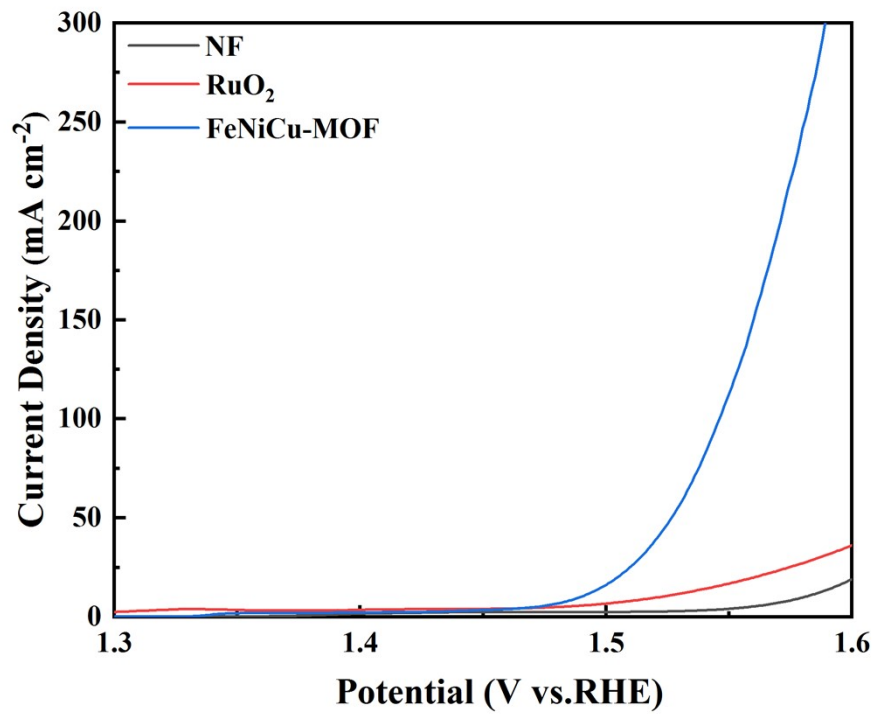


Fig. S6. LSV curves of FeNiCu-MOF, RuO₂ and bare NF electrodes in 1 M KOH.

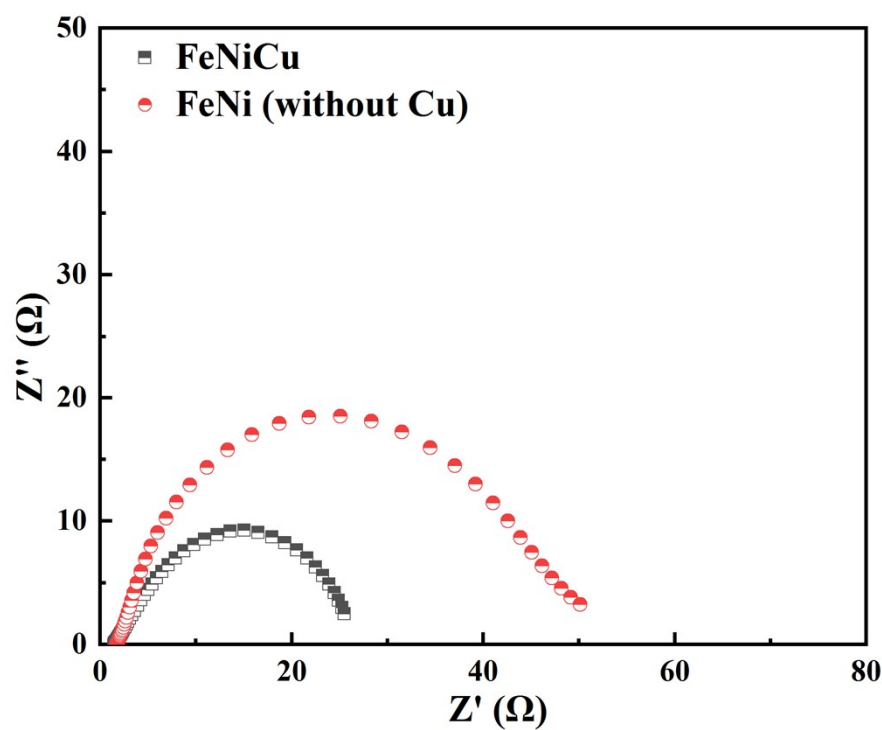


Fig. S7. EIS Nyquist plots of FeNi-MOF (without Cu) and FeNiCu-MOF.

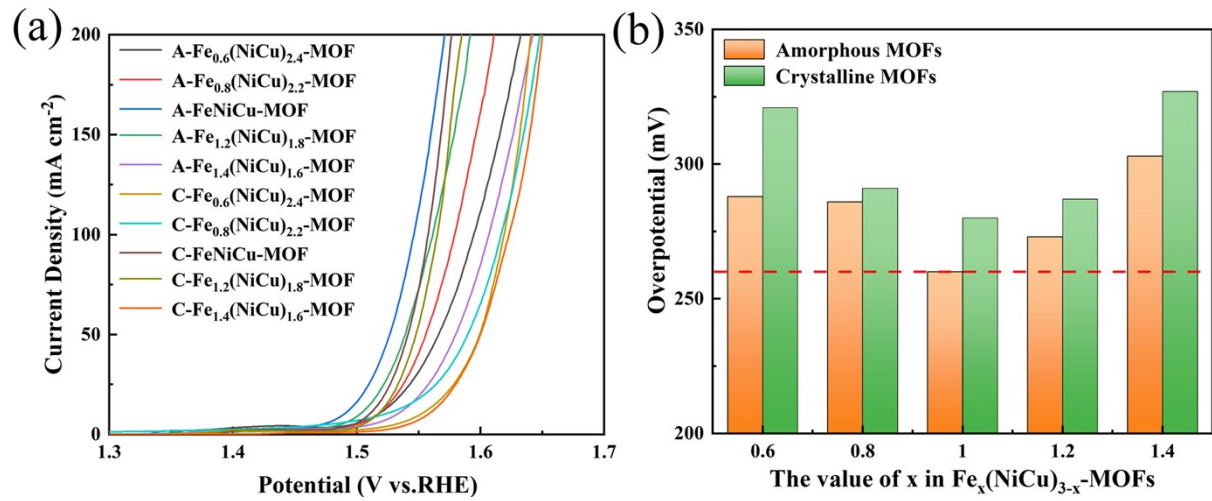


Fig. S8. OER performance of amorphous (denoted as A-) and crystalline (denoted as C-) $\text{Fe}_x(\text{NiCu})_{3-x}$ -MOFs in 1 M KOH electrolyte. (a) LSV curves. (b) Comparison of overpotential at the 10 mA/cm^2 .

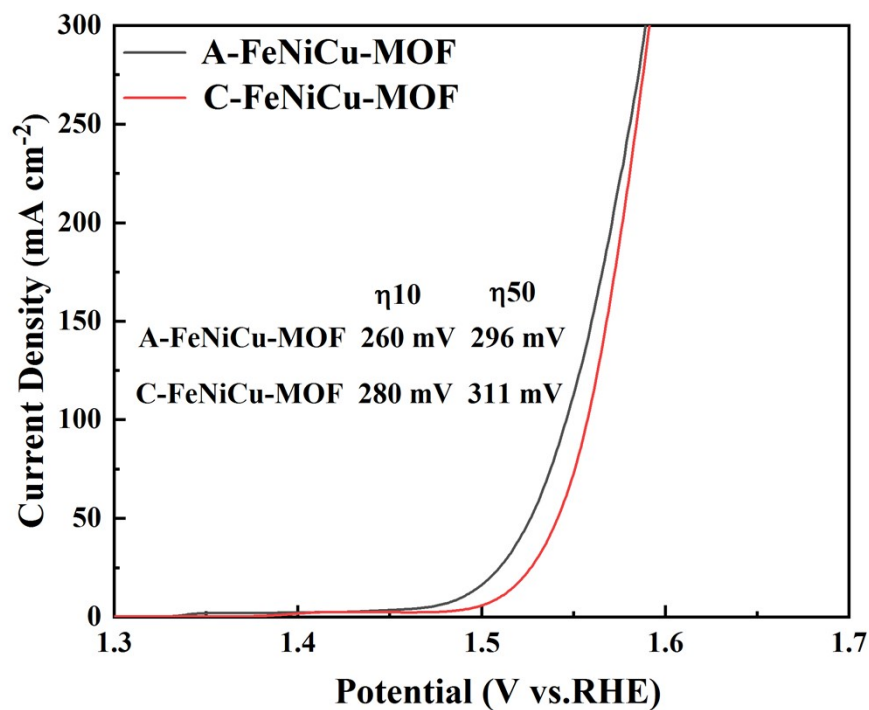


Fig. S9. LSV curves of amorphous and crystalline FeNiCu-MOF.

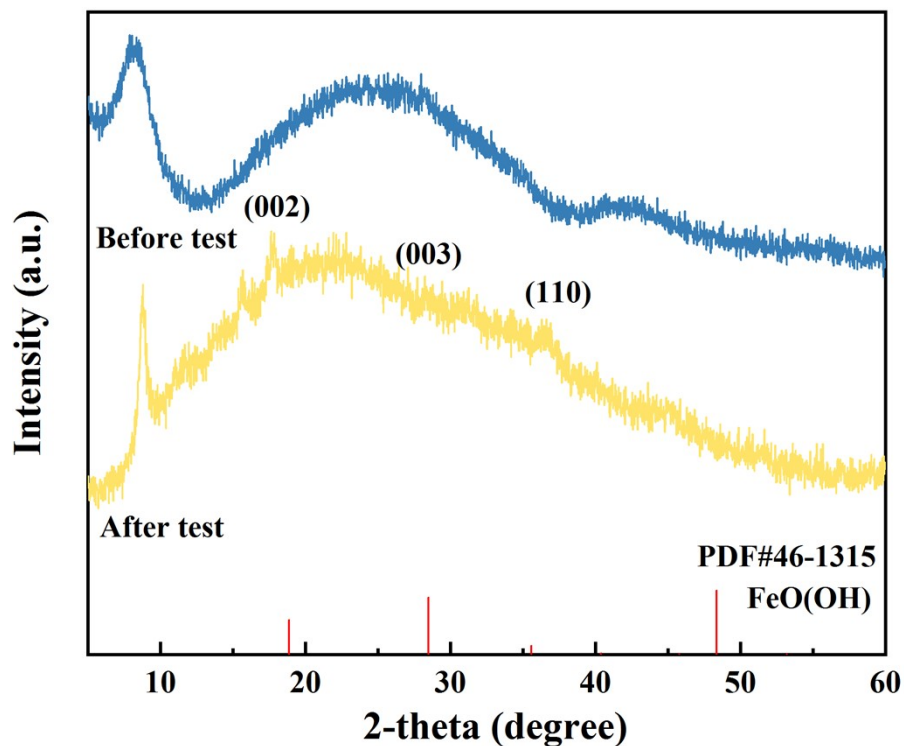


Fig. S10. XRD patterns of FeNiCu-MOF before and after the chronoamperometry test.

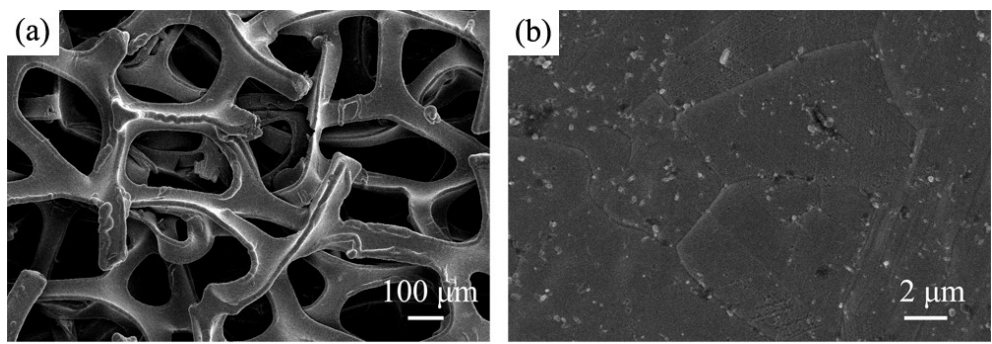


Fig. S11. (a) Low-resolution SEM of nickel foam (NF), (b) High-resolution SEM of NF.

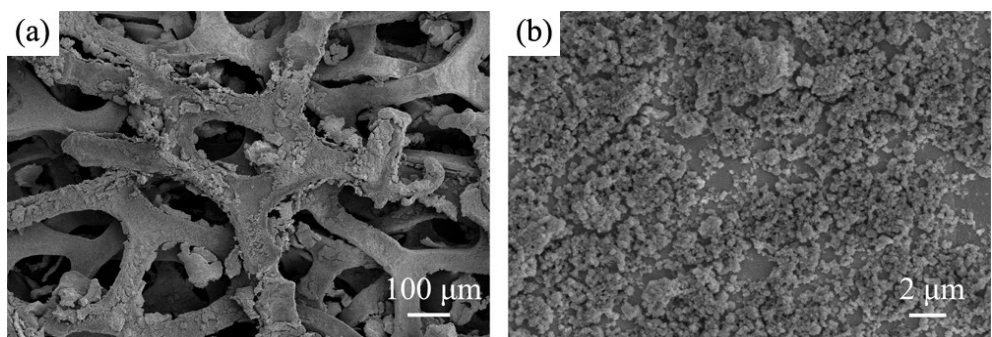


Fig. S12. (a) Low-resolution SEM of FeNiCu-MOF on NF before test, (b) High-resolution SEM of FeNiCu-MOF on NF before test.

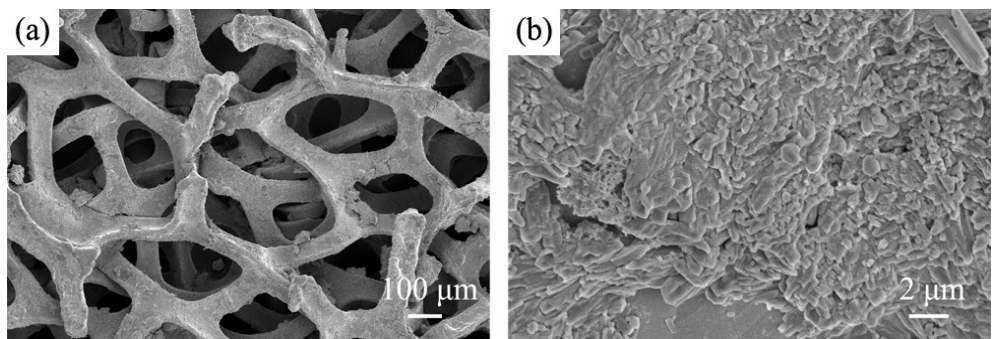


Fig. S13. (a) Low-resolution SEM of FeNiCu-MOF on NF after test, (b) High-resolution SEM of FeNiCu-MOF on NF after test.

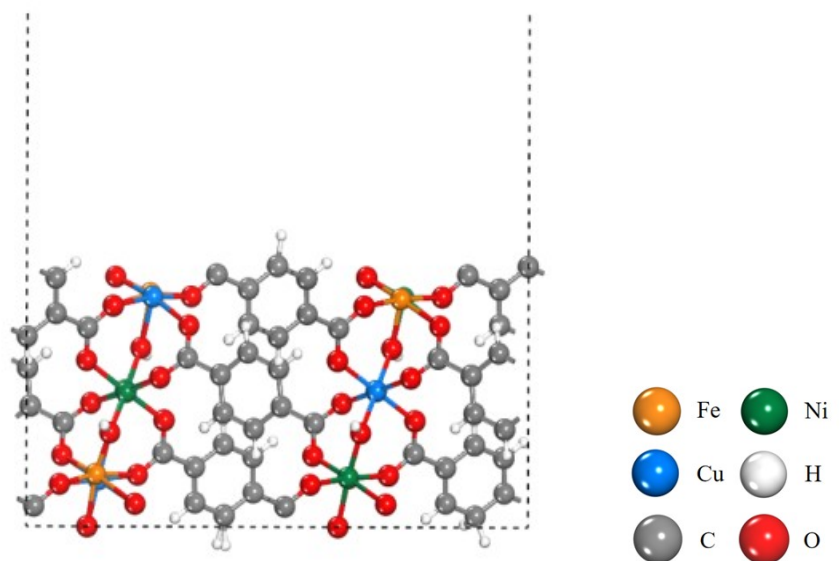


Fig. S14. Crystal plane (200) of FeNiCu-MOF structure.

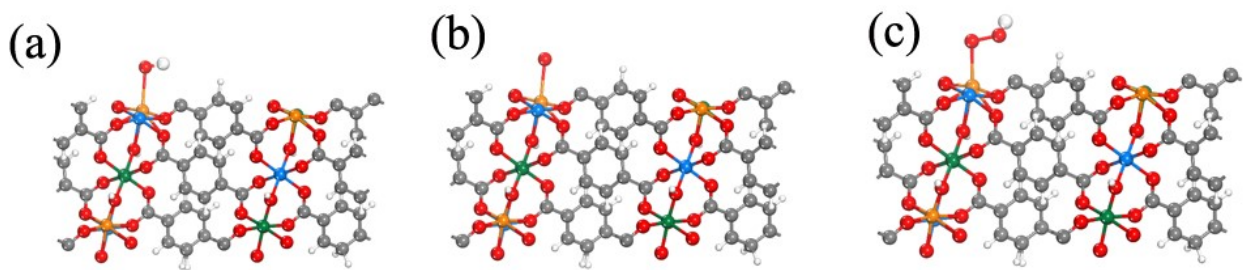


Fig. S15. Intermediate state structure of OER free energy in Fe active sites in FeNiCu-MOF structure, (a) *OH, (b) *O, (c) *OOH.

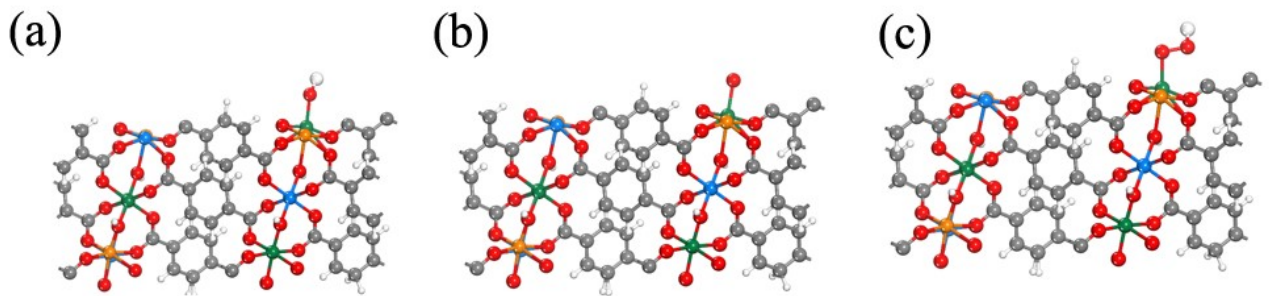


Fig. S16. Intermediate state structure of OER free energy in Ni active sites in FeNiCu-MOF structure, (a) *OH, (b) *O, (c) *OOH.

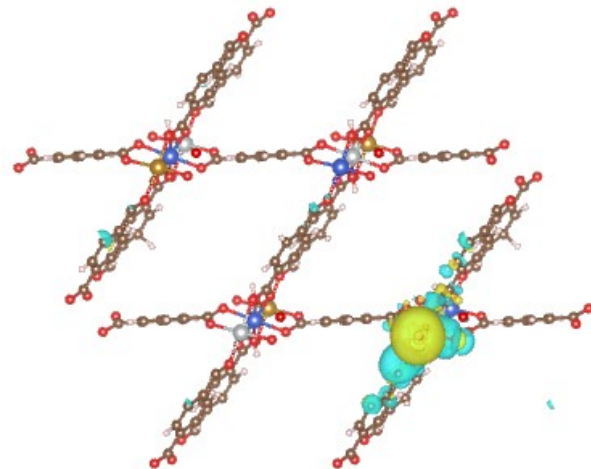


Fig. S17. Charge density difference of $^{*}\text{O}$ intermediates adsorption on the Fe sites of FeNiCu-MOF. The depletion of electrons is shown in blue and accumulation of electrons is drawn in yellow, and the isosurface is set to $0.0005 \text{ e } \text{\AA}^{-3}$.

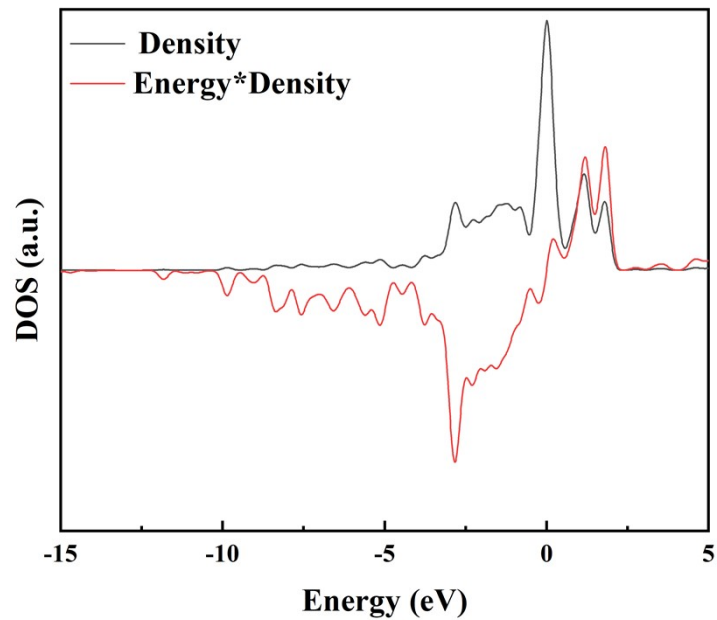


Fig. S18. Integral method for calculating the d band center of Fe atoms.

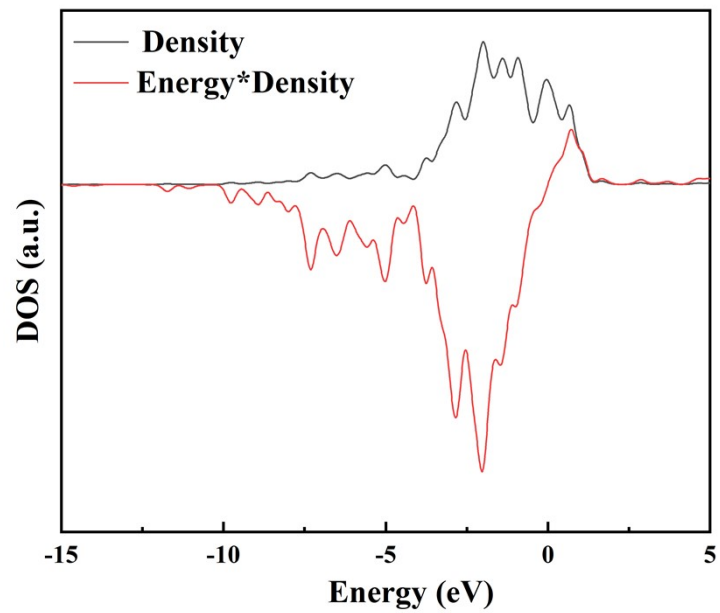


Fig. S19. Integral method for calculating the d band center of Ni atoms.

Table S1. The content of different synthetic samples.

Sample	Amount of substance (mmol)			Quality (mg)		
	FeCl ₂ ·4H ₂ O	NiCl ₂ ·6H ₂ O	CuCl ₂ ·2H ₂ O	FeCl ₂ ·4H ₂ O	NiCl ₂ ·6H ₂ O	CuCl ₂ ·2H ₂ O
Fe _{0.6} (NiCu) _{2.4}	0.15	0.3	0.3	29.8	71.3	51.1
Fe _{0.8} (NiCu) _{2.2}	0.2	0.275	0.275	39.7	65.3	46.9
FeNiCu	0.25	0.25	0.25	49.7	59.4	42.6
Fe _{1.2} (NiCu) _{1.8}	0.3	0.225	0.225	59.6	53.5	38.4
Fe _{1.4} (NiCu) _{1.6}	0.35	0.2	0.2	69.6	47.5	34.1

Table S2. BET parameters of $\text{Fe}_x(\text{NiCu})_{3-x}$ -MOFs.

Sample	S_{BET} $/ \text{m}^2 \text{ g}^{-1}$	V_{total} $/ \text{cc g}^{-1}$	$D_{\text{average}} / \text{nm}$
$\text{Fe}_{0.6}(\text{NiCu})_{2.4}$	26.1	0.114	14.0
$\text{Fe}_{0.8}(\text{NiCu})_{2.2}$	34.6	0.265	26.6
FeNiCu	40.1	0.417	36.4
$\text{Fe}_{1.2}(\text{NiCu})_{1.8}$	37.3	0.270	22.2
$\text{Fe}_{1.4}(\text{NiCu})_{1.6}$	24.6	0.170	21.5

Table S3. Comparison of overpotential of amorphous $\text{Fe}_x(\text{NiCu})_{3-x}$ -MOFs at the different current density.

Sample	Overpotential (mv)		
	10 mA cm ⁻²	30 mA cm ⁻²	50 mA cm ⁻²
$\text{Fe}_{0.6}(\text{NiCu})_{2.4}$	288±2	319±5	336±8
$\text{Fe}_{0.8}(\text{NiCu})_{2.2}$	286±2	313±6	326±6
FeNiCu	260±4	283±5	296±7
$\text{Fe}_{1.2}(\text{NiCu})_{1.8}$	273±3	296±7	309±8
$\text{Fe}_{1.4}(\text{NiCu})_{1.6}$	303±5	334±8	350±9

Table S4. OER performance comparison between the reported transition metal-based MOF and FeNiCu-MOF.

Catalysts	Substrate	Electrolyte	η_{10} (mV)	Tafel slope (mV dec ⁻¹)	Reference
FeNiCu-MOF	Ni foam	1 M KOH	260	61	This work
BrNi-MOF	Carbon paper	1 M KOH	306	79.1	1
NiFe MOF/OM-NFH	GCE	1M KOH	270	123	2
Co ₃ Fe - MOF	GCE	1M KOH	280	38	3
MOF-74-derived NiFe	Ni foam LDH	1M KOH	299	48.7	4
Ni-MOF@CNT	Ni foam	1M KOH	370	138	5
MOF-derived Mo-	GCE	1M KOH	280	63	6
Co ₃ O ₄ /CNTs					
Fe(OH) ₃ @Co-MOF-	Carbon paper	1M KOH	292	44	7
NiFe-LDH	Carbon paper	1M KOH	275	56.7	8
CoFe-MOF	GCE	1M KOH	265	44	9
CoNi _{0.3} -MOF	GCE	1M KOH	330	66	10
Ni-MOF@Fe-MOF	Ni foam	1M KOH	223	72	11
Co-MOF	GCE	1M KOH	263	74	12
MCCF/NiMn-MOFs	Carbon paper	1M KOH	280	86	13

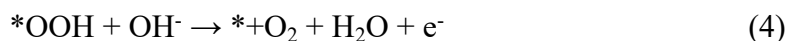
NiCo-BTC	Ni foam	1M KOH	276	56	14
MOF-derived	NC-	Carbon	1M KOH	289	103
Co/CoN	cloth				

Note: η_{10} , overpotential at 10 mA cm⁻²; GCE, Glassy-carbon electrode.

Additional statements of the computational details

Density functional theory (DFT) calculations were performed to help us understand the role of oxyhydroxide on the surface during oxygen evolution reaction. The local ordered structure of amorphous materials can replace the whole structure in DFT calculations [16,17]. According to the XRD patterns in the paper, the (200) crystal plane was selected as the adsorption surface to perform the DFT calculations, as presented in Fig. S14. Due to the above XPS results, the selection of oxyhydroxide is appropriate and it is most likely the active phase for OER catalysis [18]. Meanwhile, in order to compare the catalytic activity between Fe and Ni atoms in the optimal FeNiCu-MOF, FeOOH and NiOOH (based on the FeOOH model, Ni atoms are doped on the subsurface to replace Fe atoms) were selected as the local structures of the dynamic reconstruction of FeNiCu-MOF, respectively. It is worth noting that this is only a simplification, as the simulation of real structures of MOF are largely hindered by the complexity of the structure. The proposed simulations mainly focus on studying the local structure as well as the reaction pathways during the OER process.

All DFT calculations are to minimize all the residual forces until the convergence criterion of 0.05 eV Å⁻¹. The positions of mobile atoms (i.e., *OH, *O, and *OOH species [19]) are displaced in each direction, as shown in Fig. S15,S16. The widely used method to model the OER process was a four-electron reaction pathway in the acidic environment:



The free energy difference for different OER steps is calculated as the following:

$$\Delta G_1 = \Delta G_{*\text{OH}} \quad (5)$$

$$\Delta G_2 = \Delta G_{*\text{O}} - \Delta G_{*\text{OH}} \quad (6)$$

$$\Delta G_3 = \Delta G_{*\text{OOH}} - \Delta G_{*\text{O}} \quad (7)$$

$$\Delta G_4 = 4.92 - \Delta G_{*\text{OOH}} \quad (8)$$

The free energy of OER intermediates is defined as $\Delta G = \Delta E + \Delta E_{\text{ZPE}} - T\Delta S$, where ΔE , ΔE_{ZPE} , T and ΔS represent the reaction energy, zero-point energy, temperature (298.15 K) and the entropy, respectively [20].

$$\Delta E_{*\text{OH}} = E_{*\text{OH}} - E_* - (E_{\text{H}_2\text{O}} - 1/2E_{\text{H}_2}) \quad (9)$$

$$\Delta E_{*O} = E_{*O} - E_* - (E_{H_2O} - E_{H_2}) \quad (10)$$

$$\Delta E_{*OOH} = E_{*OOH} - E_* - (2E_{H_2O} - 3/2E_{H_2}) \quad (11)$$

where E_{*OH} , E_{*O} and E_{*OOH} are the total energies of *OH, *O and *OOH species adsorption on the slab. The E_* , E_{H_2O} , E_{H_2} are energies of slab, H₂O and H₂, respectively.

And differential charge density is obtained by the DFT. The simulation results are shown in Fig. S17. The d-band centers of the atoms are calculated by integration, as shown in Fig. S18,S19.

Reference

- [1] W. R. Cheng, S. B. Xi, Z. P. Wu, D. Y. Luan, X. W. Lou, *Sci. Adv.*, 2021, **7**, eabk0919.
- [2] X. F. Li, D. D. Ma, C. S. Cao, R. Q. Zou, Q. Xu, X. T. Wu, Q. L. Zhu, *Small*, 2019, **15**, 1902218.
- [3] W. X. Li, W. Fang, Chen Wu, K. N. Dinh, H. Ren, L. Zhao, C. T. Liu, Q. Y. Yan, *J. Mater. Chem. A*, 2020, **8**, 3658-3666.
- [4] M. Rinawati, Y. X. Wang, K. Y. Chen, M. H. Yeh, *Chem. Eng. J.*, 2021, **423**, 130204.
- [5] T. V .M. Sreekanth, G. R. Dillip, P. C. Nagajyothi, K. Yoo, J. Kim, *Appl. Catal., B*, 2021, **285**, 119793.
- [6] K. L. Lu, T. T. Gu, L. J. Zhang, Z. C. Wu, R. H. Wang, X. J. Li, *Chem. Eng. J.*, 2021, **408**, 127352.
- [7] Z. Gao, Z. W. Yu, F. Q. Liu, C. Yang, Y. H. Yuan, Y. Yu, F. Luo, *Chem. Sus. Chem.*, 2019, **12**, 4623-4628.
- [8] M. Liu, L. J. Kong, X. M. Wang, J. He, X. H. Bu, *Small*, 2019, **15**, 1903410.
- [9] Z. H. Zou, T. T. Wang, X. H. Zhao, W. J. Jiang, H. R. Pan, D. Q. Gao, C. L. Xu, *ACS Catal.*, 2019, **9**, 7356-7364.
- [10] Y. Li, Z. G. Gao, H. M. Bao, B. H. Zhang, C. Wu, C. F. Huang, Z. L. Zhang, Y. Y. Xie, Hai Wang, *J. Energy Chem.*, 2021, **53**, 251-259.
- [11] J. Zing, K. Guo, Z. Zou, M. Cai, J. Du, C. Xu, *Chem. Commun.*, 2018, **54**, 7046-7049.
- [12] Y. X. Xu, B. Li, S. S. Zheng, P. Wu, J. Y. Zhan, H. G. Xue, Q. Xu, H. Pang, *J. Mater. Chem. A*, 2018, **6**, 22070-22076.
- [13] W. R. Cheng, X. F. Lu, D. Y. Luan, X. W. Lou, *Angew. Chem. Int. Ed.*, 2020, **59**, 18234-18239.
- [14] X. Zhang, J. S. Luo, K. Wan, D. Plessers, B. Sels, J. X. Song, L. G. Chen, T. Zhang, P. Y. Tang, J. R. Morante, J. Arbiol, J. Fransaer, *J. Mater. Chem. A*, 2019, **7**, 1616-1628.
- [15] C. Guan, A. Sumboj, W. J. Zang, Y. H. Qian, H. Zhang, X. M. Liu, Z. L. Liu, D. Zhao, S. J. Pennycook, John Wan, *Energy Storage Mater.*, 2019, **16**, 243-250.
- [16] S. H. Liu, S.Z Geng, L. Li, Y. Zhang, G. M. Ren, B. L. Huang, Z. W. Hu, J. F. Lee, Y. H. Lai, Y. H. Chu, Y. Xu, Q. Shao, X. Q. Huang, *Nat. Commun.*, 2022, **13**, 1187.
- [17] X. B. Hou, Z. K. Han, X. J. Xu, D. Sarker, J. Zhou, M. Wu, Z. C. Liu, M. H. Huang, H. Q. Jiang, *Chem. Eng. J.*, 2021, **418**, 129330.
- [18] H. Shin, H. Xiao, W. A. Goddard, *J. Am. Chem. Soc.*, 2018, **140**, 6745-6748.

- [19] J. Wang, M. K. Zhang, G. L. Yang, W. W. Song, W. T. Zhong, X. Y. Wang, M. M. Wang, T. M. Sun, Y. F. Tang, *Adv. Funct. Mater.*, 2021, **31**, 2101532.
- [20] J. K. Nørskov, J. Rossmeisl, A. Logadottir, L. Lindqvist, J. R. Kitchin, T. Bligaard, H. Jónsson, *J. Phys. Chem. B.*, 2004, **108**, 17886-17892.